npj | Climate and Atmospheric Science

www.nature.com/npjclimatsci

ARTICLE OPEN

Check for updates

Human-caused long-term changes in global aridity

Rongfan Chai[1,2,6], Jiafu Mao[2,6]✉, Haishan Chen[1]✉, Yaoping Wang[3], Xiaoying Shi[2], Mingzhou Jin[3], Tianbao Zhao[4], Forrest M. Hoffman[5], Daniel M. Ricciuto[2] and Stan D. Wullschleger[2]

Widespread aridification of the land surface causes substantial environmental challenges and is generally well documented. However, the mechanisms underlying increased aridity remain relatively underexplored. Here, we investigated the anthropogenic and natural factors affecting long-term global aridity changes using multisource observation-based aridity index, factorial simulations from the Coupled Model Intercomparison Project phase 6 (CMIP6), and rigorous detection and attribution (D&A) methods. Our study found that anthropogenic forcings, mainly rising greenhouse gas emissions (GHGE) and aerosols, caused the increased aridification of the globe and each hemisphere with high statistical confidence for 1965–2014; the GHGE contributed to drying trends, whereas the aerosol emissions led to wetting tendencies; moreover, the bias-corrected CMIP6 future aridity index based on the scaling factors from optimal D&A demonstrated greater aridification than the original simulations. These findings highlight the dominant role of human effects on increasing aridification at broad spatial scales, implying future reductions in aridity will rely primarily on the GHGE mitigation.

npj Climate and Atmospheric Science (2021)4:65 ; https://doi.org/10.1038/s41612-021-00223-5

INTRODUCTION

Aridity, and associated water scarcity, is a long-term hydrologic and climatic condition, exerting pervasive influences on dynamics in human society and terrestrial ecosystems (e.g., more frequent hydrologic and ecosystem droughts, increased economic losses, decreased land carbon sink)[1–3]. Recent studies indicate that aridity, defined in terms of atmospheric supply (precipitation) and demand of water (potential evapotranspiration, PET), has increased globally during recent decades and is projected to increase significantly in the future[2,4,5]. However, uncertainty remains in the natural and anthropogenic mechanisms leading to changes in such aridity. Natural variability (e.g., Pacific Decadal Oscillation and El Niño–Southern Oscillation [ENSO]) has been found to modulate large-scale aridity via atmosphere-ocean feedbacks and atmospheric teleconnections[6,7]; however, the natural variability alone cannot explain increasing aridification at long timescales[8–10]. Overall, anthropogenic greenhouse gas emissions can enhance global precipitation[11] and modify stomatal conductance and plant water use[12], likely relieving the aridity stress; however, the ubiquitous increase in PET associated with greenhouse gas-induced warming may aggravate the aridity[13]. Thus, the net greenhouse gas effects on global aridity remain uncertain and require further research[1,12]. Given the much shorter residence time and more complex effects of aerosols than those of greenhouse gas emissions[14], aerosols have been identified as the second-largest anthropogenic driver in the Earth system, partially offsetting the greenhouse gas effects on drying[15,16]. Nevertheless, the identification of aerosol aridity effects is challenging because of their heterogeneous spatial distribution and direct and indirect interactions with hydrological cycles[17,18].

Defined as the ratio of annual precipitation to PET, the aridity index (AI) has been widely used to characterize the degree of meteorological drought[4,5,13,19]. Compared with other meteorological drought indices (e.g., Standardized Precipitation Index and Palmer Drought Severity Index), the AI is more climatically suitable for the characterization of aridity/wetness condition and for the classification of climate and vegetation over certain regions. Moreover, the AI has been shown to closely correlate with the changes of other drought types (e.g., hydrologic drought, agricultural drought, ecosystem drought), although it represents background climatological aridity more than specific drought events[19–21]. Previous AI studies typically used a single set of observation[5,22] or merely model results[23–25], thereby limiting the robustness of their findings. Investigations of AI changes were also primarily focused on the roles played by meteorological variables, such as precipitation and PET[4,23,26], without strict quantification of the contributions from major human and natural forcings. Moreover, little effort has been made to constrain future AI simulations using multiple historical observations[5,27], which could induce significant uncertainty in the AI projections.

In this study, we aim to comprehensively disentangle the human fingerprints from natural internal variability for the AI changes during the 1965 to 2014 period. To decrease the uncertainty of long-term AIs, we developed a collection of historical AI products based on multisource observational precipitation and reanalysis PET data sets (see Methods and Supplementary Note 1). The PET data were derived from the modified Penman–Monteith algorithm[28] that includes the effects of temperature, humidity, solar radiation, wind speed, and atmospheric CO_2 concentrations. For both the global scale and two hemispheres, a formal detection and attribution (D&A) analysis was conducted to separate the individual contributions from human activities and natural variability using optimal fingerprinting methods[29,30], the new AI products, and the latest factorial experiments from the Coupled Model Intercomparison

[1]Key Laboratory of Meteorological Disaster, Ministry of Education/International Joint Research Laboratory of Climate and Environment Change/Collaborative Innovation Center on Forecast and Evaluation of Meteorological Disasters, and School of Atmospheric Sciences, Nanjing University of Information Science and Technology (NUIST), Nanjing, China. [2]Environmental Sciences Division and Climate Change Science Institute, Oak Ridge National Laboratory, Oak Ridge, TN, USA. [3]Institute for a Secure and Sustainable Environment, University of Tennessee, Knoxville, TN, USA. [4]Key Laboratory of Regional Climate-Environment Research for Temperate East Asia, Institute of Atmospheric Physics, Chinese Academy of Sciences, Beijing, China. [5]Computational Sciences and Engineering Division and Climate Change Science Institute, Oak Ridge National Laboratory, Oak Ridge, TN, USA. [6]These authors contributed equally: Rongfan Chai, Jiafu Mao ✉email: maoj@ornl.gov; haishan@nuist.edu.cn

Project phase 6 (CMIP6). These CMIP6 ensemble experiments (see Supplementary Note 2) comprise those driven by historical anthropogenic and natural forcings (ALL), greenhouse gas forcing only (GHG), natural forcing only (NAT), aerosol forcing only (AER), and preindustrial control (piControl). We further applied the D&A-derived scaling factors, which indicate the amount by which the amplitude of the model-simulated responses to forcing must be altered to be consistent with the observations[29–31], to correct the future aridity trends under different CMIP6 Shared Socioeconomic Pathways (e.g., SSP3 − 7.0 and SSP5 − 8.5).

RESULTS

Spatiotemporal patterns of historical aridity

The observed AI trends (OBS), averaged across 12 combinations of source precipitation and PET datasets (see Methods), showed negative (drier) trends over the vast majority of North America, Western Europe, central South America, and South Africa. Positive (wetter) trends were shown to be scattered over north Africa, India, tropical southeast Asia, and northwest Australia (Fig. 1a). Such more widespread drying (61.2% of the global area in OBS) than wetting patterns were generally captured by the ALL experiments (57.8% of the global area showed drying), albeit with over or underestimated magnitudes (Fig. 1b). However, a notable difference of the ALL results from the OBS occurred over central Africa, possibly from the African wetting produced by the AER forcing (Supplementary Fig. 1c) (see Discussion). The model biases in the simulated responses of precipitation and PET to the ALL forcing may have also contributed to the ALL-OBS differences in various regions, including the Sahel region, the Arabian Peninsula, South America, and Australia (Supplementary Fig. 1). In terms of percentage changes in AI, the OBS (Supplementary Fig. 2a) showed greater percentage increases or decreases in northern Africa, western Asia, western Australia than the other parts of the world, which was likely due to the dryness (i.e., low climatological AI values) of these regions (Supplementary Fig. 2c). The ALL simulations generally agreed with the observations, except for failing to reproduce the higher decreased changes over western Asia (Supplementary Fig. 2b). In contrast to the ALL simulations, the NAT simulations had much weaker trend magnitudes of AI than those of both the OBS and ALL simulations, and little inter-model agreement on the signs of the trends (Fig. 1c). The average AI trends under the NAT forcing were slightly positive over central North America and central Eurasia, and mainly negative over Africa, East Asia, and Australia (Fig. 1c). The AI changes simulated by the anthropogenic forcing (ANT, obtained by subtracting the NAT from the ALL simulations; Fig. 1d) resembled the ALL results and generally agreed with the OBS (Fig. 1a), indicating that the combined anthropogenic effects dominated the AI changes, especially the extensive drying trends. For individual anthropogenic effects, the GHG determined long-term drying tendencies across most regions around the globe (Fig. 1e), whereas the AER caused evident drying over western Europe and wetting across other continents, especially Africa, East Asia, and Australia (Fig. 1g).

For the global AI anomalies (relative to 1973 to 2002), the OBS showed an overall downward trend (-0.032 ± 0.018 per 50 yr), reproduced by both the ALL and ANT ensemble simulations (-0.022 ± 0.0067 and -0.017 ± 0.011 per 50 yr, respectively) (the time series is shown in Fig. 2a, and the entire distribution of trends in Supplementary Fig. 3). The observed drying tendency, however, was not captured in magnitude or sign by the NAT, AER, or the non-GHG anthropogenic (ANTnoGHG, obtained by subtracting the GHG from the ANT simulations) simulations (-0.0047 ± 0.0037, 0.0034 ± 0.0097, and -0.0059 ± 0.0090 per 50 yr, respectively; Supplementary Fig. 3). Both the GHG and the non-AER anthropogenic (ANTnoAER, obtained by subtracting the AER from the ANT simulations) experiments simulated the global AI trends comparable to the OBS and ALL, confirming the controlling role of greenhouse gases on the AI changes within the anthropogenic influences (Supplementary Figs. 3 and 4). For the two hemispheres, both showed long-term drying trends, with a larger magnitude of decrease for the Northern Hemisphere (NH) (-0.038 ± 0.020 mm mm^{-1} per 50 yr) than for the Southern Hemisphere (SH) (-0.018 ± 0.011 mm mm^{-1} per 50 yr) (Fig. 2b, c and Supplementary Fig. 3). These hemisphere-scale observational drying trends were largely reproduced by the simulations that included GHG in the forcings (i.e., ALL, ANT, GHG, ANTnoAER) but not by the simulations that excluded GHG in the forcings (i.e., NAT, AER, ANTnoGHG) (Supplementary Figs. 3, 5, and 6). The magnitudes of drying were slightly smaller in the ALL and ANT simulations (-0.022 ± 0.0067 and -0.017 ± 0.011 per 50 yr, respectively) than those in the OBS (-0.032 ± 0.018 per 50 yr) for the global- and NH-averaged AIs (Supplementary Fig. 3). Such underestimation of drying trends by the ALL and ANT simulations for the global and NH resulted mainly from the wetting trends over central Africa (Fig. 1).

D&A of aridity changes

Using the above-described global- and hemispheric-averaged time series of AI, we performed D&A analyses of the aridity changes by regressing[29–31] the model simulations driven with different external forcings onto the OBS time series averaged over all combinations of precipitation and PET data for the period 1965–2014. The regressions included fitting using each forcing (1-forcing analyses; e.g., ALL, ANT, GHG, AER, and NAT), two forcings (2-forcing analyses; e.g., ANT and NAT), and three forcings (3-foricng analyses; e.g., AER, ANTnoAER and NAT and GHG, ANTnoGHG, and NAT). The regression procedure thus produces regression coefficients, i.e., scaling factors, that indicate the difference between model-simulated responses and the observations. We considered a forcing detectable if the 90% confidence interval of the scaling factor lies above zero, and attributable if this confidence interval also includes one. As sensitivity analysis, the D&A regressions were performed using two regression methods (optimal least squares [OLS][30,31] and total least squares [TLS][29]) and on a few different setups of CMIP6 ensemble members (All, Limited, 3-member, and Uniform, see the Methods and caption of Fig. 3 for details).

Based on the OLS–estimated scaling factors for the OBS, at the global level, the ALL and ANT forcings were detectable and attributable in 1- forcing (one forcing) and 2-forcing (joint forcings) analyses; the GHG forcing was detectable in 1- and 3-forcing (joint forcings) analyses, but not consistently attributable in 3-forcing analysis; the ANTnoAER forcing, which includes the GHG and the ANTnoGHGAER forcing (obtained by subtracting the GHG and AER simulations from the ANT simulations; examples include land use and land cover change, ozone), was detectable and attributable in 3-forcing analysis; the AER forcing was not consistently detectable in 1-forcing analysis but was detectable in 3-forcing analysis; the ANTnoGHG forcing, which includes the AER forcing and the ANTnoGHGAER forcing, was not detectable; the NAT forcing was not detectable except in one case (the 3-forcing analysis AER-ANTnoAER-NAT, Limited CMIP6 models) (Fig. 3a). In the NH, the D&A conclusions for ALL, ANT, GHG, ANTnoAER, and ANTnoGHG were identical to the global results; the AER forcing was not consistently detectable in 1-forcing analysis but was detectable or detectable and attributable in 3-forcing analysis; the NAT forcing was only detectable in some combinations of CMIP6 models and a number of analyzed forcings (Fig. 3c). In the SH, the D&A results for ALL, ANT, GHG, ANTnoAER, and ANTnoGHG were the same as the global conclusions; the AER forcing was not detectable in 1-forcing analysis but was detectable and attributable in the 3-forcing analysis; the NAT forcing was not detectable (Fig. 3e). These results demonstrate a significant presence of

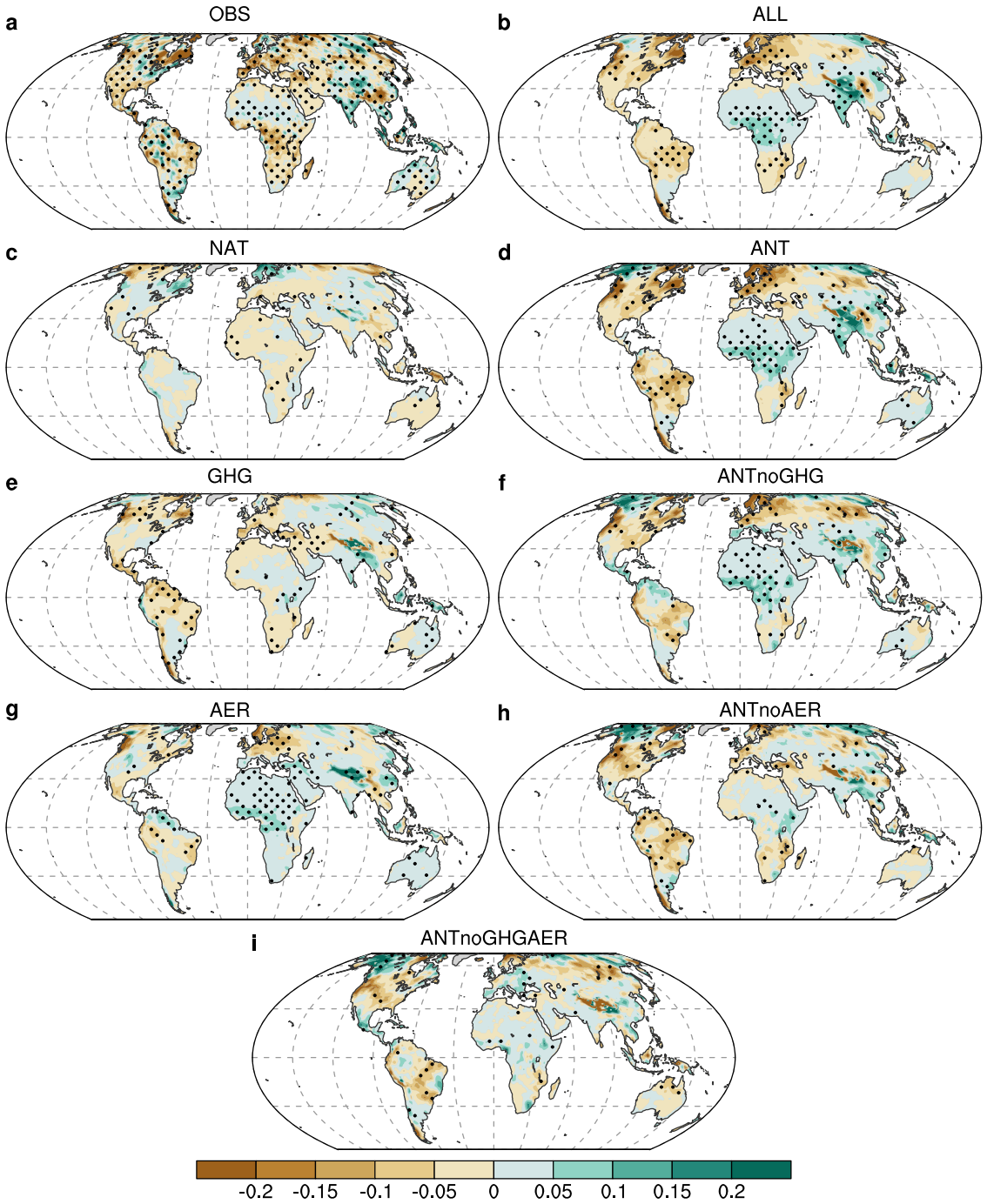

Fig. 1 Spatial distribution of AI trends for 1965 to 2014. Spatial distribution of the linear trends of 5-yr mean annual AI (per 50 yr) in the mean of observations (OBS) (**a**), and CMIP6 simulations with ALL (**b**), NAT (**c**), and ANT (**d**), GHG (**e**), ANTnoGHG (**f**), AER (**g**), ANTnoAER (**h**), and ANTnoGHGAER forcings (**i**). The dot indicates at least 70% of the simulation members agreeing on the direction of the trend at that point.

anthropogenic signals, which are likely a combination of GHG and AER in the global, NH-, and SH-averaged AI. The consistently detectable or detectable and attributable forcings (i.e., ALL, ANT, GHG, and ANTnoAER) contributed to negative (i.e., drying) trends in the global, NH-, and SH-averaged AIs (Fig. 3b, d, and f). The AER forcing in 3-forcing analysis contributed to positive (i.e., wetting) trends in the global, NH-, and SH-averaged AIs (Fig. 3b, d, and f).

The broadscale AI D&A results based on OLS mostly did not change with the choice of CMIP6 models (e.g., all available CMIP6 models [All] or only the CMIP6 models with at least three ensemble members [3-member]), with the exceptions being the AER forcing in the 1-forcing analysis, and the NAT forcing in some of the 1- or 3-forcing analysis for the global and NH-averaged AI (Fig. 3a and c). Applying an alternative regression-based D&A method, TLS, generally yielded higher uncertainty intervals for the scaling factors than the OLS method, but the ALL and ANT forcings remained detectable and attributable for the global, NH-, and SH-averaged AIs in the 1-forcing analyses, and the GHG forcing remained detectable or detectable and attributable for the global- and NH-averaged AIs in 1- and 3-forcing analyses (Supplementary Fig. 7).

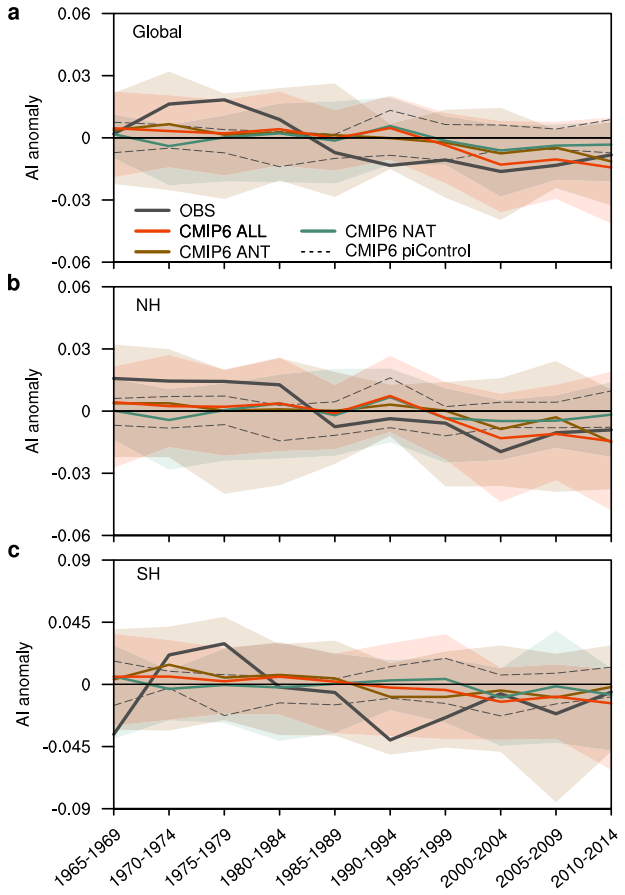

Fig. 2 Observed and simulated 1965 to 2014 time series of AI anomalies (relative to 1973 to 2002). The 5-yr mean annual AI anomalies overland of the globe (**a**), NH (**b**), and SH (**c**) for the mean of observations (OBS) and CMIP6 simulations accounting for ALL, NAT, and ANT forcings. The ensemble means for each set of forcings are given in red, green, and brown solid lines for ALL, NAT, and ANT, respectively. The observation means are indicated with solid black lines. Red, green, and brown shading represent the 5–95% ranges for ALL, NAT, and ANT ensembles, respectively. The gray dashed lines represent the 5%–95% ranges for the range of variability for the piControl.

Additional sensitivity analysis on the D&A analysis included applying the OLS and TLS methods on the observed AI time series derived from different precipitation data sets (Climatic Research Unit [CRU], Climate Prediction Center [CPC], Global Precipitation Climatology Centre [GPCC], University of Delaware [UDEL]) and different reanalysis-based PET data sets (Global Land Data Assimilation System [GLDAS], NOAA-CIRES Twentieth Century Reanalysis [20CR], ERA5) (Supplementary Figs. 8−15). Supplementary Table 1 provides a further summary of the D&A results shown in Fig. 3 and Supplementary Figs. 7−15, i.e., across the various combinations of methods, observations, and CMIP6 models. Three of the precipitation data sets (CRU, GPCC, CPC) generally resulted in D&A of the ALL, GHG, AER, and ANTNoAER forcings in the global and NH-averaged AI, whereas the UDEL-precipitation data set generally resulted in only the detection of these forcings. The use of the CPC-precipitation-based observed AI in the D&A resulted in no detection of the ANT forcing in the NH-averaged AI (Supplementary Table 1), which was caused by relatively large uncertainty intervals in the scaling factors, and the point estimates of the ANT scaling factors generally had similar values to the other precipitation data sets (Supplementary Figs. 7−15). The use of the GLDAS-reanalysis-based observed AI in the D&A generally resulted in D&A of the ALL, ANT, GHG, AER, and ANTNoAER forcings in the global and NH-averaged AI. The use of the 20CR reanalysis-based observed AI in the D&A did not result in the detection of the ALL or ANT forcings. The use of the ERA-5-reanalysis-based observed AI in the D&A did not result in the detection of the ALL forcing in the global averaged AI. For the SH-averaged AI, the various precipitation and reanalysis data sets resulted in similar D&A conclusions to the OBS.

Future evolutions of aridity

Under the SSP3 − 7.0 and SSP5 − 8.5, the projected global and hemispheric AIs were simulated to continue to decrease in the twenty-first century (Fig. 4). The faster AI declining rates were associated with SSP5 − 8.5 (-0.030 ± 0.026, -0.030 ± 0.031, and -0.033 ± 0.018 per 50 yr for the globe, NH, and SH, respectively), whereas the slower changes were projected by SSP3 − 7.0 (-0.027 ± 0.015, -0.025 ± 0.018, and -0.033 ± 0.012 per 50 yr for the globe, NH, and SH, respectively). Spatially, the original CMIP6 simulations showed consistently drying trends over central North America, central South America, southern Europe and southern Africa under both SSP3 − 7.0 and SSP5 − 8.5 scenarios (Supplementary Fig. 16). The regions with changes toward wetting conditions mainly scattered over high latitudes of NH, central and South Asia, central Africa, and southern South America (Supplementary Fig. 16). Wide-ranging temporal variations between different SSPs or within the same SSP suggested large uncertainties occurred in the original projected trends of future drying. Compared with the original projected trends, the corrected trends in the global, NH-, and SH-averaged AI, obtained by multiplying the best estimates of, respectively, global, NH-, or SH-scaling factors from the historical D&A analysis on the ALL forcing, showed even faster drying rates and larger drying trends for all focus regions (Fig. 4 and Supplementary Table 2). In the SH, such higher AI magnitudes and related wider ranges of AI trends for the corrected projections than the original ones were mainly caused by the large regression-based D&A scaling factors and associated uncertainty intervals (Figs. 3e and 4c).

DISCUSSION

Previous studies have identified intensified global aridification based on aridity analyses or other drought variables[7–9,32], including the Palmer Drought Severity Index, soil moisture index, and streamflow. We also found significant decreases in AI (i.e., drying trends) broadly consistent in sign and magnitude across the globe and two hemispheres (Fig. 2 and Supplementary Fig. 2). Traditionally, areas where the AI is less than 0.65 are classified as dryland and are further divided into subtypes of hyper-arid ($AI < 0.05$), arid ($0.05 \le AI < 0.2$), semiarid ($0.2 \le AI < 0.5$) and dry subhumid ($0.5 \le AI < 0.65$) regions. The spatially widespread decreases in AI (>60% of the global area, on the order of ~0.1 per 50 years; Fig. 1) would not have much impact over extremely dry and wet regions (e.g., Sahara Desert and Southeast Asia) but may trigger the transition from wetter to drier types and then increase the risks of land degradation and desertification.

We further examined the key role that human activity, especially greenhouse gas emissions, played in strengthening aridity over the study period (Fig. 3). For the globe, NH, and SH, the GHG forcing was consistently detected or detected and attributed (Fig. 3, Supplementary Table 1), and the GHG simulations well captured the decreasing AI trends in the OBS (Fig. 2 and Supplementary Figs. 3–6). Such AI decreases driven by elevated greenhouse gas emissions were mainly caused by the increase in air temperature, as detailed in Supplementary Note 3 and Supplementary Fig. 17, implying that the land precipitation increase could not keep pace with the growing evaporative demand associated with greenhouse gas–dominated warming[13]. For the globe, NH, and SH, the AER forcing was also frequently

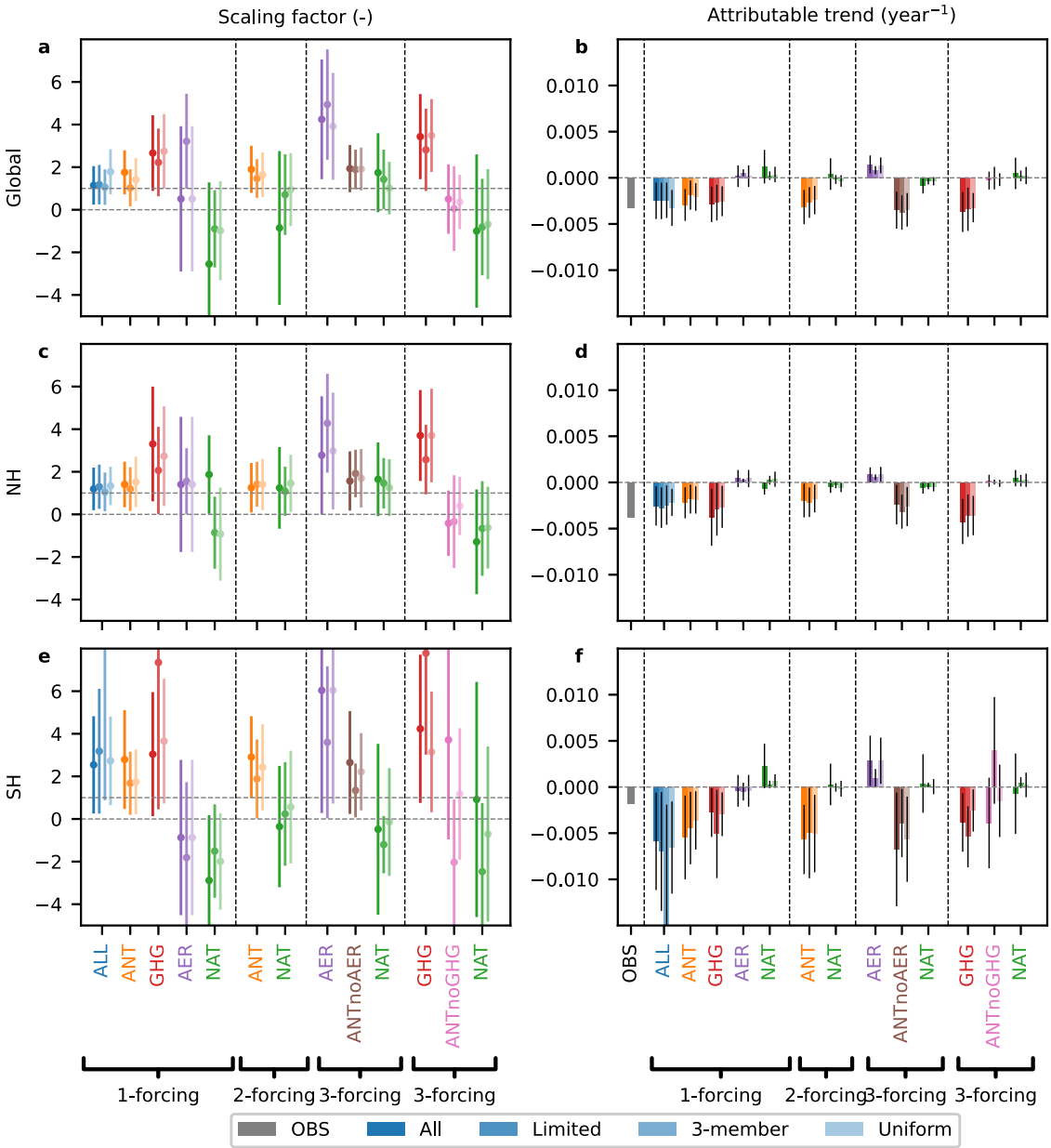

Fig. 3 D&A analysis for the 1965 to 2014 time series of AI anomalies. The scaling factors and observed and attributable trends for global- (**a**, **b**), NH- (**c**, **d**), and SH-averaged (**e**, **f**) AIs were estimated using the OLS D&A method and the average of observations. The scaling factors were estimated one by one (1-forcing) and jointly (2- and 3-forcing). Error bars show 90% confidence intervals for the scaling factors. "ALL" used all the available CMIP6 models, "Limited" used the models that have both piControl and target forcing (e.g., ALL and ANT) simulations, "3-member" used models with large ensembles (≥3 members), and "Uniform" used models that have piControl and all the forcings (ALL, GHG, AER, NAT) simulations. The 3-member case was only displayed for the ALL forcing because it was identical to the All case for the other forcings.

detected or detected and attributed (Fig. 3, Supplementary Table 1). Through the absorption and scattering of incoming solar radiation, aerosols reduce incoming solar radiation at the land surface and thus offset part of the aridity resulting from greenhouse gas emissions–induced warming, which is consistent with the identified positive contributions of AER to the global, NH-, and SH-averaged AI trends (Fig. 3). However, because of the indirect aerosol effects, such as the aerosol-cloud interactions through microphysical processes[17,33], the increase in anthropogenic aerosol emissions may lead to reduced large-scale precipitation and, hence, enhanced aridity[15,34]. Notably, aerosol emissions have exhibited strong spatiotemporal heterogeneity with a shift from developed to developing countries since the 1970s[18]. Such a transition further exerted complicated effects on regional and remote aridity via altered circulation patterns and associated changes in precipitation and PET[35–37]. For example, the AER simulations produced evident wetting trends over Africa, especially central Africa, with the reduction of PET and increase of precipitation both contributing to such positive AI trends (Fig. 1g and Supplementary Fig 18).

The similarity in the D&A results between GHG and ANTnoAER, including when the two forcings were estimated from the same set of CMIP6 models (e.g., the Uniform setting), suggests that the effects of the ANTnoGHGAER forcing were small compared with the GHG forcing. The general lack of detection of the ANTnoGHG forcing may be because the effects of the AER forcing were

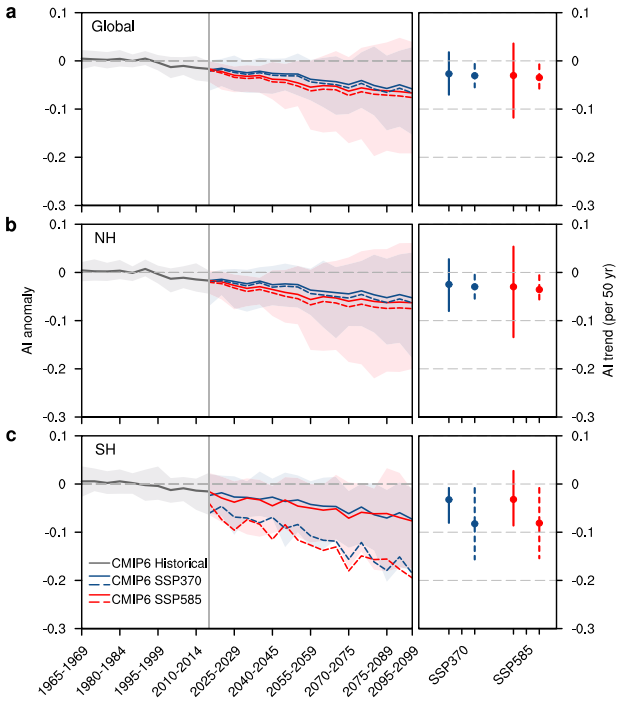

Fig. 4 Time series (left) and trends (right) of AI anomalies (relative to 1973 to 2002) for 1965 to 2099. Time series and linear trends (per 50 yr) of 5-yr mean annual AI anomalies over the globe (**a**), NH (**b**), and SH (**c**) for CMIP6 simulations. The ensemble means of historical ALL simulations are indicated with solid grey lines. The ensemble means for original future projection are given in dark blue and red solid lines for SSP3 − 7.0 and SSP5 − 8.5 ensembles, respectively, with blue and red shading represent the 5–95% ranges. The dashed lines indicate the corrected AI anomalies using the ALL scaling factors from 1-forcing analyses. The vertical solid and dashed bars show the trend uncertainty spread of original and corrected AI anomalies for SSP3 − 7.0 and SSP5 − 8.5 ensembles as labelled, respectively, with the dots indicating the mean values.

smaller than the GHG forcing, albeit detectable, and were counteracted by the ANTnoGHGAER forcing over the majority of the global land surface (Fig. 1i and Supplementary Figs. 4−6).

As shown in Supplementary Table 1, the results of D&A somewhat depended on the method of analysis, the number of forcings analyzed, and observational and model products. Compared with the OLS method, the TLS D&A method rarely detected the GHG forcing in the SH-averaged AI and had much higher uncertainty in the scaling factors (Supplementary Table 1 and Supplementary Figs. 7, 9, 13, and 15). These differences may be because the TLS statistical model has more degrees of freedom than OLS[29,30], and because the TLS model may correctly estimate the uncertainty intervals of the scaling factors when the signal-to-noise ratio is low in the D&A[29]. Considering the generally low signal-to-noise ratios in hydrological variables, this study mainly adopted OLS to derive robust results but used TLS as auxiliary. The detection of the AER forcing in 3-forcing analysis but not 1-forcing analysis (Fig. 3 and Supplementary Fig. 7) may be because the AER forcing explained a relatively small fraction of variability in the historical AI. Therefore, in 1-forcing analysis, the residuals of the OLS formula may be too large to pass the residual consistency test of the D&A analysis[30,31], resulting in un-detection. For different combinations of CMIP6 ensemble simulations, the inconsistencies in D&A results existed mainly in the weak forcings (AER and NAT), and the results on ALL, ANT, GHG, and ANTnoAER were consistent (Fig. 3 and Supplementary Fig. 7). The uncertainty across different combinations of precipitation and reanalysis data sources was high in the global and NH-averaged AI, and low in the SH-averaged AI. The use of UDEL-precipitation-based AI differed from other precipitation-based AI data sets in detecting but not attributing most of the analyzed forcings, likely because the UDEL data set has a stronger decreasing trend during the study period than other precipitation products[9]. The differences across the reanalysis data sets occurred on the ALL and ANT forcings, whereas the GHG and AER forcings were generally detected or detected and attributed for all three reanalysis data sets. The lack of detection of the ALL and ANT forcings in the 20CR reanalysis in the global and NH-averaged AI may be because the 20CR reanalysis only assimilated surface pressure[38] and was less realistic than the other reanalysis data sets. The lack of detection of the ALL forcing in the ERA5 reanalysis in the global and NH-averaged AI may be because the ERA5-based AI, similar to the UDEL-based AI, showed large decreases during the study period (Supplementary Fig. 19). Despite these uncertainties, each precipitation or reanalysis data set resulted in the detection of at least two of the ALL, ANT, GHG, and AER forcings with the OLS method, and at least one with the TLS method, supporting the significant existence of anthropogenic signals.

In addition to the above-mentioned uncertainty sources, the D&A analysis may be influenced by the choice of window sizes for the spatial and temporal averaging of the gridded AI values. The temporal window size (5-year averaging) selected in this study was to remove some interannual variability (e.g., ENSO) while retaining a sufficiently large number of data points (10) for the D&A analysis. However, the current averaging window did not preclude the influence from oscillations that have a characteristic time scale longer than 5 year (e.g., the Pacific Decadal Oscillation). The spatial window size (global and hemispheric) selected in this study also omitted a more detailed investigation of AI driving mechanisms across smaller regions or particular ecosystems, deserving further in-depth D&A analysis.

The model-projected trends of land aridity in the twenty-first century may contain significant uncertainty as shown in this study (Fig. 4) and previous work[1,4,26,38,39]. To constrain the changes of future aridity, various bias-correction algorithms were tested[5,27,40,41] and the resulting corrections were proved to be sensitive to the choice of methods and input observational data sets[5,41,42]. For example, a projected high frequency of aridification could become less prevalent after the correction without considering the PET effects[40,43]; contrasting sign and magnitude in aridity changes may be obtained[5,41] after the constraints accounting for the effects of evaporative demand. For this study, the future-corrected AIs were calculated by multiplying the original SSP AIs with the best scaling factors estimated from the historical D&A analyses. The underlying assumption was that the fractional biases in the model responses to external forcings would largely stay constant over time[44]. This approach, however, can be mainly applied onto global and regional changes under scenarios where radiative forcings increase over time, such as the SSP3 − 7.0 and SSP5 − 8.5, but not all the SSP cases[45,46]. Such process-based corrections resulted in more negative AI trends than the original CMIP6 results, calling again for the need to be prepared for a likely increased risk of more arid conditions in the future, especially for the high-emission scenarios[5]. However, AI mainly characterizes the meteorological drought in an integrative way rather than all drought features that could be captured by other aridity or drought metrics (e.g., vapor pressure deficit, soil moisture, river flow, vegetation productivity). Consistent with previous estimates, the updated PET algorithm for AI calculation in this study produced decreased AI magnitudes (less aridification) by considering the CO_2 physiological effects under elevated CO_2 conditions (see Supplementary Note 1)[12,47]. Nevertheless, to achieve a more comprehensive understanding of aridification changes and their uncertainties, other processes (e.g., land use/land cover change effects, land-atmosphere feedback, land-ocean

warming contrast) in the climate and terrestrial ecosystems should be quantified further[13,47–49].

In summary, we have high confidence that the intensified aridifications across broad spatial scales were caused primarily by human activity between 1965 and 2014. Within the verified anthropogenic effects, the GHG forcing dominated the long-term observed drying tendencies around the globe, as well as two hemispheres; and the AER forcing mitigated these drying trends as a secondary affecting factor of AI. Stronger future aridity changes projected by the constrained CMIP6 simulations suggest more pressing environmental challenges that will likely face society.

METHODS

Development of observational AI products

AI, the ratio of annual precipitation to PET, represents a balance between the moisture supply and demand[4,5], and was used in this study to quantify the degree of aridity. The decrease of the AI over a certain region indicates that the climate is getting drier. To reduce the historical AI uncertainties associated with different choices of precipitation and PET data sets, we derived an ensemble of AI products based on the best available observational precipitation and reanalysis PET data sets. The precipitation data were from the CRU, the CPC National Centers of the Environmental Prediction, the UDEL, and the GPCC. Climate variables (e.g., temperature, radiation, specific humidity, wind speed, air pressure) involved in PET calculations were obtained from selected reanalysis products, including the 20CR, the ECMWF ERA-5, and the GLDAS. All the data sets used cover the world's land area excluding Antarctica and were interpolated into 0.5° by 0.5° spatial resolution for the 1965 to 2014 period. In total, 12 members of observation-based AI were produced by considering all possible combinations of precipitation and PET products (Supplementary Table 3).

D&A

Formal D&A analysis was implemented using the OLS regression method[29,36] (see Supplementary Note 4), which estimates the scaling factors between the observation and simulated responses under one or more different forcings. A scaling factor that is significantly greater than 0 based on a 90% confidence interval is interpreted as that the forcing is detectable (called "detectable" in the Results and Discussion sections), and a scaling factor statistically indistinguishable from 1 is interpreted as the forcing being detectable and the observed signal being attributable to the forcing (called "detectable and attributable" in the Results and Discussion sections). The method also involves residual consistency tests to ensure the variances of the regression residuals are consistent with model internal variability. The D&A method was applied onto the AI observations and CMIP6 AI under one forcing (1-forcing analysis), and two or three forcings jointly (2- and 3-forcing analyses). To account for observational uncertainty, the 12-member AI observations were grouped and averaged according to the source of precipitation data (CRU, GPCC, UDEL, CPC), the source of reanalysis-based PET (GLDAS, 20CR, ERA5), and over all the combinations of precipitation and PET data (OBS). To test the robustness of the D&A results to the choice of methods, the TLS regression method[28] was performed on all the AI observations and simulations (see Supplementary Note 5) in addition to the OLS method. To account for the uncertainty in simulated AI uncertainties, the D&A analysis was conducted on the using all the available CMIP6 models (All), the CMIP6 models that have both piControl and target forcing (ALL, ANT, GHG, AER, NAT, ANTnoAER, or ANTnoGHG) simulations (Limited), the CMIP6 models with large ensembles (≥3 members) only (3-member), and the CMIP6 models that have piControl and all the forcings (ALL, ANT, GHG, AER, NAT, ANTnoAER) and ANTnoGHG) simulations (Uniform).

DATA AVAILABILITY

The data sets used in this study are derived from published sources (Supplementary Note 2 and Supplementary Table 3). The data that support the plots and other findings of this study are available from the corresponding authors upon request.

CODE AVAILABILITY

The code to carry out the current analyses is available from the corresponding authors upon request.

Received: 20 June 2021; Accepted: 6 December 2021;
Published online: 21 December 2021

REFERENCES

1. Huang, J. et al. Dryland climate change: Recent progress and challenges. *Rev. Geophys.* **55**, 719–778 (2017).
2. Koutroulis, A. G. Dryland changes under different levels of global warming. *Sci. Total Environ.* **655**, 482–511 (2019).
3. Moreno-Jiménez, E. et al. Aridity and reduced soil micronutrient availability in global drylands. *Nat. Sustain.* **2**, 371–377 (2019).
4. Feng, S. & Fu, Q. Expansion of global drylands under a warming climate. *Atmos. Chem. Phys.* **13**, 10081–10094 (2013).
5. Huang, J., Yu, H., Guan, X., Wang, G. & Guo, R. Accelerated dryland expansion under climate change. *Nat. Clim. Change* **6**, 166–171 (2016).
6. Qian, C. & Zhou, T. Multidecadal variability of North China aridity and its relationship to PDO during 1900–2010. *J. Clim.* **27**, 1210–1222 (2014).
7. Dai, A. Increasing drought under global warming in observations and models. *Nat. Clim. Change* **3**, 52–58 (2013).
8. Bonfils, C. J. et al. Human influence on joint changes in temperature, rainfall and continental aridity. *Nat. Clim. Change* **10**, 726–731 (2020).
9. Trenberth, K. E. et al. Global warming and changes in drought. *Nat. Clim. Change* **4**, 17–22 (2014).
10. Bonfils, C. et al. Competing influences of anthropogenic warming, ENSO, and plant physiology on future terrestrial aridity. *J. Clim.* **30**, 6883–6904 (2017).
11. Allen, M. R. & Ingram, W. J. Constraints on future changes in climate and the hydrologic cycle. *Nature* **419**, 228–232 (2002).
12. Swann, A. L., Hoffman, F. M., Koven, C. D. & Randerson, J. T. Plant responses to increasing CO_2 reduce estimates of climate impacts on drought severity. *Proc. Natl Acad. Sci. USA* **113**, 10019–10024 (2016).
13. Sherwood, S. & Fu, Q. A drier future? *Science* **343**, 737–739 (2014).
14. Kaufman, Y. J., Tanré, D. & Boucher, O. A satellite view of aerosols in the climate system. *Nature* **419**, 215–223 (2002).
15. Polson, D., Bollasina, M., Hegerl, G. C. & Wilcox, L. J. Decreased monsoon precipitation in the Northern Hemisphere due to anthropogenic aerosols. *Geophys. Res. Lett.* **41**, 6023–6029 (2014).
16. Wu, P., Christidis, N. & Stott, P. Anthropogenic impact on Earth's hydrological cycle. *Nat. Clim. Change* **3**, 807–810 (2013).
17. Chung, E. S. & Soden, B. J. Hemispheric climate shifts driven by anthropogenic aerosol–cloud interactions. *Nat. Geosci.* **10**, 566–571 (2017).
18. Wang, Y., Jiang, J. H. & Su, H. Atmospheric responses to the redistribution of anthropogenic aerosols. *J. Geophys. Res. Atmos.* **120**, 9625–9641 (2015).
19. Girvetz, E. H. & Zganjar, C. Dissecting indices of aridity for assessing the impacts of global climate change. *Clim. Change* **126**, 469–483 (2014).
20. Dai, A., Zhao, T. & Chen, J. Climate change and drought: A precipitation and evaporation perspective. *Curr. Clim. Change Rep.* **4**, 301–312 (2018).
21. Guan, X., Huang, J. & Guo, R. Changes in aridity in response to the global warming hiatus. *J. Meteorol. Res.* **31**, 117–125 (2017).
22. Lickley, M. & Solomon, S. Drivers, timing and some impacts of global aridity change. *Environ. Res. Lett.* **13**, 104010 (2018).
23. Fu, Q. & Feng, S. Responses of terrestrial aridity to global warming. *J. Geophys. Res. Atmos.* **119**, 7863–7875 (2014).
24. Fu, Q., Lin, L., Huang, J., Feng, S. & Gettelman, A. Changes in terrestrial aridity for the period 850–2080 from the Community Earth System Model. *J. Geophys. Res. Atmos.* **121**, 2857–2873 (2016).
25. Lin, L., Gettelman, A., Xu, Y. & Fu, Q. Simulated responses of terrestrial aridity to black carbon and sulfate aerosols. *J. Geophys. Res. Atmos.* **121**, 785–794 (2016).
26. Scheff, J. & Frierson, D. M. Terrestrial aridity and its response to greenhouse warming across CMIP5 climate models. *J. Clim.* **28**, 5583–5600 (2015).
27. Ficklin, D. L., Abatzoglou, J. T., Robeson, S. M. & Dufficy, A. The influence of climate model biases on projections of aridity and drought. *J. Clim.* **29**, 1269–1285 (2016).
28. Yang, Y. et al. Hydrologic implications of vegetation response to elevated CO_2 in climate projections. *Nat. Clim. Change* **9**, 44–48 (2019).
29. Allen, M. R. & Stott, P. A. Estimating signal amplitudes in optimal fingerprinting, part I: Theory. *Clim. Dynam.* **21**, 477–491 (2003).
30. Allen, M. R. & Tett, S. F. B. Checking for model consistency in optimal fingerprinting. *Clim. Dynam.* **15**, 419–434 (1999).
31. Ribes, A., Planton, S. & Terray, L. Application of regularised optimal fingerprinting to attribution. Part I: Method, properties and idealised analysis. *Clim. Dynam.* **41**, 2817–2836 (2013).
32. Marvel, K. et al. Twentieth-century hydroclimate changes consistent with human influence. *Nature* **569**, 59–65 (2019).

33. Wilcox, L. J., Highwood, E. J. & Dunstone, N. J. The influence of anthropogenic aerosol on multi-decadal variations of historical global climate. *Environ. Res. Lett.* **8**, 024033 (2013).
34. Singh, D., Bollasina, M., Ting, M. & Diffenbaugh, N. S. Disentangling the influence of local and remote anthropogenic aerosols on South Asian monsoon daily rainfall characteristics. *Clim. Dynam.* **52**, 6301–6320 (2019).
35. Wang, Y. et al. Reduced European aerosol emissions suppress winter extremes over northern Eurasia. *Nat. Clim. Change* **10**, 225–230 (2020).
36. Undorf, S., Bollasina, M. A. & Hegerl, G. C. Impacts of the 1900–74 increase in anthropogenic aerosol emissions from North America and Europe on Eurasian summer climate. *J. Clim.* **31**, 8381–8399 (2018).
37. Westervelt, D. M. et al. Connecting regional aerosol emissions reductions to local and remote precipitation responses. *Atmos. Chem. Phys.* **18**, 12461–12475 (2018).
38. Compo, G. P. et al. The twentieth century reanalysis project. *Q. J. R. Meteorol. Soc.* **137**, 1–28 (2011).
39. Zhao, T. & Dai, A. Uncertainties in historical changes and future projections of drought. Part II: model-simulated historical and future drought changes. *Clim. Change* **144**, 535–548 (2017).
40. Johnson, F. & Sharma, A. What are the impacts of bias correction on future drought projections? *J. Hydrol.* **525**, 472–485 (2015).
41. Koutroulis, A. G. Dryland changes under different levels of global warming. *Sci. Total Environ.* **655**, 482–511 (2019).
42. Nguyen, H., Mehrotra, R. & Sharma, A. Can the variability in precipitation simulations across GCMs be reduced through sensible bias correction? *Clim. Dynam.* **49**, 3257–3275 (2017).
43. Aryal, Y. & Zhu, J. On bias correction in drought frequency analysis based on climate models. *Clim. Change* **140**, 361–374 (2017).
44. Allen, M. R., Stott, P. A., Mitchell, J. F., Schnur, R. & Delworth, T. L. Quantifying the uncertainty in forecasts of anthropogenic climate change. *Nature* **407**, 617–620 (2000).
45. Stott, P. A. & Forest, C. E. Ensemble climate predictions using climate models and observational constraints. *Philos. Trans. R. Soc. A* **365**, 2029–2052 (2007).
46. Gidden, M. et al. Global emissions pathways under different socioeconomic scenarios for use in CMIP6: A dataset of harmonized emissions trajectories through the end of the century. *Geosci. Model Dev.* **12**, 1443–1475 (2019).
47. Lian, X. et al. Multifaceted characteristics of dryland aridity changes in a warming world. *Nat. Rev. Earth Environ.* **2**, 232–250 (2021).
48. Zipper, S. C., Keune, J. & Kollet, S. J. Land use change impacts on European heat and drought: remote land-atmosphere feedbacks mitigated locally by shallow groundwater. *Environ. Res. Lett.* **14**, 044012 (2019).
49. Berg, A. et al. Land–atmosphere feedbacks amplify aridity increase over land under global warming. *Nat. Clim. Change* **6**, 869–874 (2016).

ACKNOWLEDGEMENTS

This research was supported by the Natural Science Foundation of China (42088101), the program of China Scholarships Council (No. 201908320504), and the Reducing Uncertainties in Biogeochemical Interactions through Synthesis and Computation Science Focus Area project in the Earth and Environmental Systems Sciences Division of the Biological and Environmental Research Office in the US Department of Energy (DOE) Office of Science. This manuscript has been authored by UT-Battelle LLC under Contract No. DE-AC05-00OR22725 with the US Department of Energy (DOE). The US government retains and the publisher, by accepting the article for publication, acknowledges that the US government retains a nonexclusive, paid-up, irrevocable, worldwide license to publish or reproduce the published form of this manuscript, or allow others to do so, for US government purposes. DOE will provide public access to these results of federally sponsored research in accordance with the DOE Public Access Plan (http://energy.gov/downloads/doe-public-access-plan).

AUTHOR CONTRIBUTIONS

J.M. and H.C. conceived the research; R.C., Y.W., J.M., and H.C. performed the analysis; and R.C., J.M., H.C., Y.W., X.S., M.J., T.Z., F.H., D.R., and S.W. wrote the paper; R.C. and J.M. contributed equally to this work.

COMPETING INTERESTS

The authors declare no competing interests.

ADDITIONAL INFORMATION

Supplementary information The online version contains supplementary material available at https://doi.org/10.1038/s41612-021-00223-5.

Correspondence and requests for materials should be addressed to Jiafu Mao or Haishan Chen.

Reprints and permission information is available at http://www.nature.com/reprints

Publisher's note Springer Nature remains neutral with regard to jurisdictional claims in published maps and institutional affiliations.

Open Access This article is licensed under a Creative Commons Attribution 4.0 International License, which permits use, sharing, adaptation, distribution and reproduction in any medium or format, as long as you give appropriate credit to the original author(s) and the source, provide a link to the Creative Commons license, and indicate if changes were made. The images or other third party material in this article are included in the article's Creative Commons license, unless indicated otherwise in a credit line to the material. If material is not included in the article's Creative Commons license and your intended use is not permitted by statutory regulation or exceeds the permitted use, you will need to obtain permission directly from the copyright holder. To view a copy of this license, visit http://creativecommons.org/licenses/by/4.0/.

© The Author(s) 2021